Texture Evolution of Bainitic Steels Processed from Nickel Lateritic Ores: A Neutron-Diffraction Investigation

Andika W. Pramono[1]*, Tri Hardi Priyanto[2], Fatayalkadri Citrawati[3], Efendi Mabruri[3], M. Yunan Hasbi[3], Andon Insani[2]

[1]Research Center for Advanced Materials – National Research and Innovation Agency – KST B. J. Habibie Puspiptek, Tangerang Selatan 15314, Banten, Indonesia
[2]Research Center for Radiation Detection and Nuclear Analysis Tech-nology – National Research and Innovation Agency – KST B. J. Habibie Puspiptek, Tangerang Selatan 15314, Banten, Indonesia
[3]Research Center for Metallurgy – National Research and Innovation Agency – KST B. J. Habibie Puspiptek, Tangerang Selatan 15314, Banten, Indonesia

Abstract. This study investigated the texture evolution of bainitic steel samples processed from lateritic nickel ores with varying heat treatment times. The samples were austenitized, air-cooled, and subjected to bainitic heat treatment at 532°C for 15 and 30 minutes. Scanning electron microscopy (SEM) analysis revealed that the sample treated at 532°C for 15 minutes, developed bainitic plates within the austenitic matrix due to the relatively rapid air cooling. Conversely, the sample, heat-treated at 532°C for 30 minutes, exhibited a combination of bainitic and pearlitic microstructures. Neutron diffraction analysis using software showed moderate-to-weak textures in both samples, indicating dislocation polygonization resulting from prolonged heat treatment. The results suggest that further research is needed to investigate the texture evolution of bainitic steels from nickel lateritic ores after plastic deformation. This work contributes to understanding the microstructural characteristics of bainitic steel derived from nickel lateritic ores, which may have significant implications for the production and application of these steels in the future.

1 Introduction

Nickel laterite ores currently account for 60% of the global nickel supply, with 71% being used for stainless steel production, 5% for batteries, and 24% for other applications [1]. However, projections suggest that by 2025, the demand for nickel laterite ores will shift towards 62% for stainless steel, 21% for batteries, and 17% for other uses [2]. Two main types of nickel laterite ores exist, i.e., limonite [3] and silicate [4]. Limonite ore is primarily processed into ferronickel and nickel matte for iron and steel production. Nickel pig iron (NPI) is an intermediate product between nickel laterite ores and steel, in contrast to pig iron derived from iron ores [5-8]. Through alloying and heat treatment, various types of steel and cast irons can be produced during or after the steel-making process.

Bainitic steel, with its plate-like microstructures, is one of the types of steel commonly used in the automotive industry. The bainitic structure was first mentioned by Edgar Bain [9, 10] and consists mainly of Fe3C (cementite) and dislocation-rich α-ferrite. Upper bainite forms during slow to moderate cooling in the temperature range of 400°C - 550°C on the time-temperature-transformation (TTT) diagram, whereas lower bainite forms at 250°C - 400°C [11, 12]. As the bainite content increases up to 50%, the hardness and strength of steel remain steady and increase by about 30% afterward [13]. Previous investigations have explored the texture crystallography of bainite structures in iron-ore-based steels, including the texture evolutions of bainitic steels through various isothermal and thermomechanical treatments and interactions with martensitic structures during mechanical deformation [14-18].

The motivation for this research is the increasing demand for nickel lateritic ores as a source of nickel for stainless steel and battery production and the significance of bainitic steel in the automotive industry. This study's novelty lies in investigating the texture crystallography of bainitic steel derived from nickel lateritic ores, an area that has not been extensively studied compared to bainitic steels based on iron ores. Additionally, using neutron diffraction instead of x-ray diffraction for texture measurement provides a new approach to studying bainitic steel microstructures.

The primary objective of this study is to examine the influence of variations in heat treatment time on the texture crystallography of bainitic steels obtained from nickel lateritic ores. The texture observations were analyzed using recalculated pole figures (RPFs), inverse pole figures (IPFs), and orientation distribution functions (ODFs). By providing a deeper understanding of the microstructural characteristics of bainitic steels derived from nickel lateritic ores, the results of this investigation may have significant implications for the production and application of these steels in the future.

* Corresponding author: andi010@brin.go.id

2 Materials and Methods

The as-cast nickel lateritic low carbon steel material with the composition of Fe-0.3C-3.03Ni-2.23Al was cut into two pieces with the dimensions of 1.2 x 1.2 x 1.0 cm each. Both pieces were austenitized at 945°C for 10 minutes and air-cooled. One piece was subsequently heat-treated at 532°C for 15 minutes and air-cooled (sample code: U2-8-15), whereas the other was at 532°C for 30 minutes and air-cooled (sample code: U2-8-30).

Both samples U2-8-15 and U2-8-30 were each mounted, ground, polished, and etched according to standard metallography procedure before the scanning electron microscopy/energy dispersive X-ray spectrometry (SEM/EX) analysis. The utilized etching solution at the end of metallography was nital. The SEM/EDX observations and analyses were conducted using Thermofisher Quanta 650.

Neutron diffraction was conducted on samples U2-8-15 and U2-8-30 using diffractometer neutron texture (DN2) with the neutron wavelength (λn) of 1.2799 Å. The neutron beam was generated from the nuclear reactor facility of G. A. Siwabessy at the B. J. Habibie Science and Technology Park of Puspiptek, Tangerang Selatan, Indonesia. The diffraction angles of 2θ were scanned in the interval of 20° - 105°. Data for pole figures were measured within the range of $0° \leq \phi \leq 90°$ and $0° \leq \chi \leq 90°$. ϕ indicates the sample rotation at 2θ diffraction angles, whereas the sample tilting at 2θ Bragg's diffraction angle. θ is half of Bragg's diffraction angles.

Fig. 1 shows the coordinate systems for X-ray or neutron diffraction. X, Y, and Z are the axes for the sample coordinate system, of which they are correspondingly symbolized by X = H1 (horizontal-1 direction), Y = H2 (horizontal-2 direction), and Z = V1 (vertical-1 direction). It was necessary to delineate the coordinate system of samples U2-8-15 and U2-8-30 with the notations H1, H2, and V1 since they did not experience plastic deformation. The usual notations of RD (rolling direction), TD (transverse direction), and ND (normal direction) for the sample coordinate system were not used as a consequence of zero plastic deformation. Meanwhile, x, y, and z are the axes for the crystallography coordinate system whose designations are frequently x = [100], y = [010], and z = [001]. The results of neutron diffraction were then refined using the MAUD (materials analysis using diffraction) program, before being manifested into RPFs, IPFs, and ODFs using the LaboTex software. Due to low neutron flux and limited operation of a nuclear reactor, the pole figure characterization range was constrained into $\phi = 90°$ and tilting $\chi \leq 90°$ resulting in quarter pole figures. This is possible for materials with high symmetry such as cubic crystal structures with orthorhombic sample symmetry. Other than cubic crystal structure, it may reach 360°.

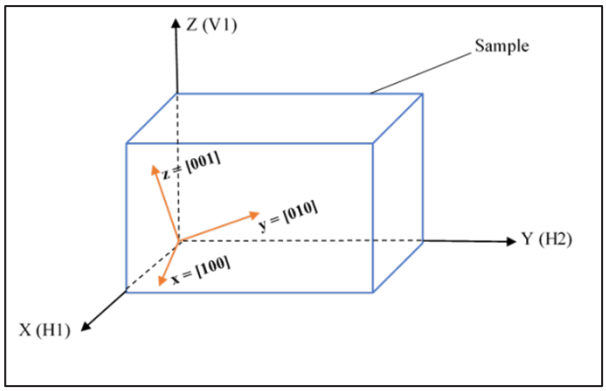

Fig. 1. The coordinate systems for samples U2-8-15 and U2-8-30. The crystallography coordinate system is indicated by the red arrows (x-y-z), whereas the sample coordinate system is by black arrows (X-Y-Z).

3 Result and Discussion

3.1 SEM/EDX Analysis

Figs. 2A and 2B show the microstructures of samples U2-8-15 and U2-8-30 at 2500 x magnification respectively. Since the samples were as-cast and not yet deformed, their microstructures showed no elongated grains or phases.

Sample U2-8-15 was heat-treated at 532°C for 15 minutes and then air-cooled. Bainitic plates (bp) appeared at the expense of the relatively smooth matrix phase of austenite (RA), as shown in Fig. 2A. With the heat treatment at 532°C for 15 minutes, the time-temperature-transformation (TTT) diagram suggested the occurrence of bainite and pearlite transformations, as suggested by Fig. 3 [19]. However, the cooling rate was relatively fast due to air cooling, which might suppress the formation of pearlite to some extent. With the given cooling rate, bainite formation was more likely than pearlite. Bainite is a microstructure that forms at intermediate cooling rates and consists of fine, needle-like structures. It is a transformation product of austenite [20]. Depending on the cooling rate and transformation kinetics, some retained austenite might be present. Retained austenite is a metastable phase that remains untransformed due to insufficient time or cooling rate [21, 22]. The air cooling was not rapid enough to allow the significant formation of martensites.

Sample U2-8-30 (Fig. 2B) was heat-treated at 532°C for 30 minutes and then air-cooled. The longer duration increased the likelihood of phase transformations, including bainite and pearlite. Similar to sample U2-8-15, bainite formation was probable due to the intermediate cooling rate. The longer time at 532°C increased the likelihood of bainite transformation. The extended duration might allow some pearlite to form. Pearlite consists of alternating layers of ferrite and cementite and forms at slower cooling rates compared to bainite [23, 24].

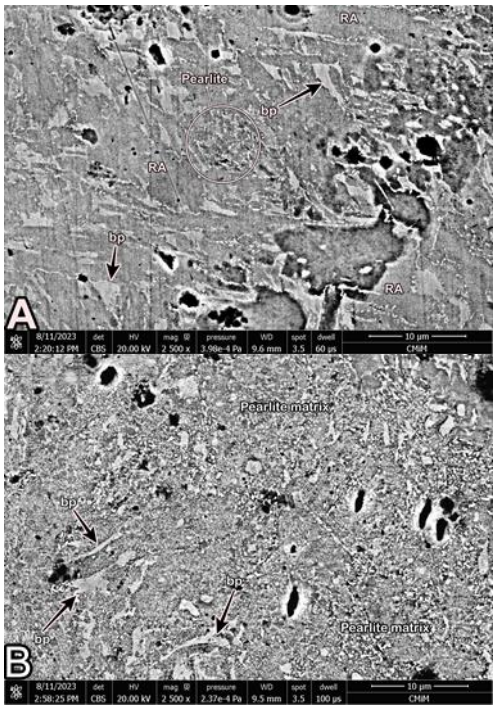

Fig. 2. Microstructures of: A. Sample U2-8-15, and B. Sample U2-8-30. In sample U2-8-15, bainitic plates (bp) occurred at the expense of the retained austenitic (RA) matrix. In sample U2-8-30, fewer bainitic plates (bp) took place at the significant pearlitic matrix.

The result of the EDX line-scanning analysis of sample U2-8-15 is shown in Fig. 4, Fig. 5, and Table 1, whereas sample U2-8-30 in Fig. 6, Fig. 7, and Table 2. The EDX analysis of sample U2-8-15 indicated the composition (in wt%) of Fe = 87.40, C = 7.83, Al = 0.89, Ni = 2.69, and Si = 1.19. The EDX composition (in wt%) of sample U2-8-30 revealed the content of Fe = 87.90, C = 7.50, Al = 1.14, Ni = 2.39, and Si = 1.06. The iron content in both samples is the highest, which is expected since these are steel samples. The slightly higher iron content in U2-8-30 suggests that there might be a higher proportion of untransformed ferrite or retained austenite in this sample due to the longer heat treatment. The carbon content is relatively consistent between the two samples. Carbon is a key element in determining the hardness and strength of steel [25, 26]. Both samples contained aluminum, which is an alloying element added for specific purposes, such as improved oxidation resistance [27, 28], enhanced strength and toughness [29, 30], as well as improved weldability [31, 32]. The slightly higher aluminum content in U2-8-30 could indicate a more complete transformation to secondary phases like bainite or pearlite. Nickel was present in both samples. It's often used in steel alloys to improve toughness, corrosion resistance, and heat resistance [33, 34]. The higher nickel content in U2-8-15 might influence its microstructure. Silicon was also present in both samples. Silicon can influence the steel's properties and its behavior during heat treatment. The silicon present in the samples likely has multiple origins, including impurities in raw materials and its role as a deoxidizer during steel production [35].

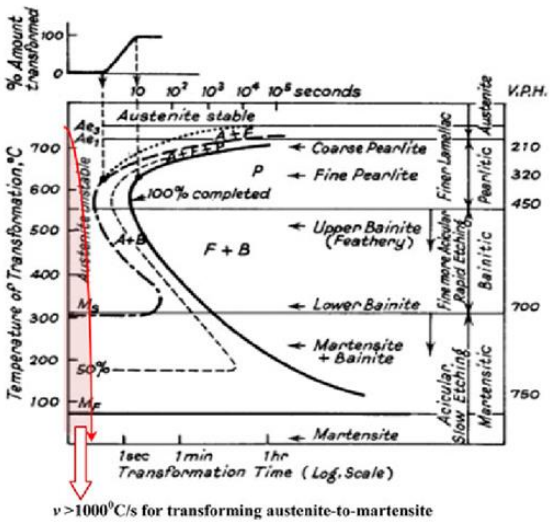

Fig. 3. TTT-diagram of 0.65% carbon steel [19].

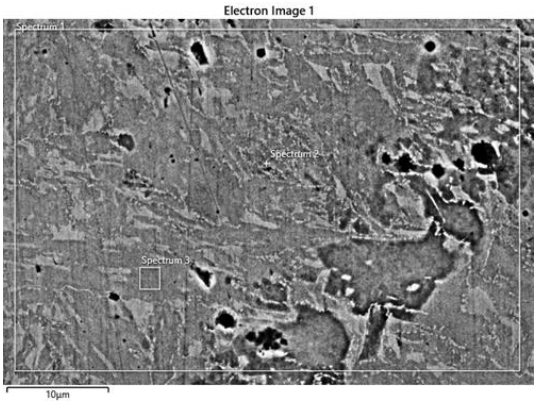

Fig. 4. Area of EDX spectrum (Spectrum1) for sample U2-8-15.

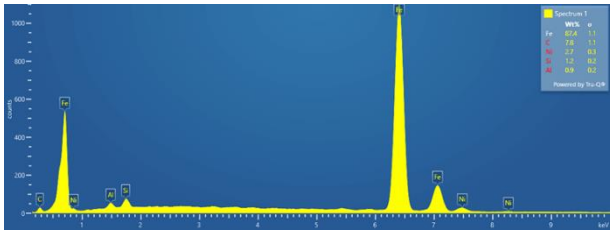

Fig. 5. EDX spectrum of sample U2-8-15.

Table 1. EDX composition of sample U2-8-15.

Element	Line Type	Weight %	Weight % Sigma	Atomic %
C	K series	7.83	1.13	27.89
Al	K series	0.89	0.17	1.40
Si	K series	1.19	0.15	1.82
Fe	K series	87.40	1.14	66.93
Ni	K series	2.69	0.33	1.96
Total		100.00		100.00

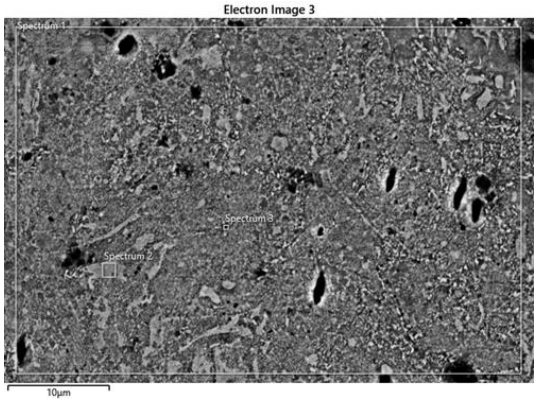

Fig. 6. Area of EDX spectrum (Spectrum1) for sample U2-8-30.

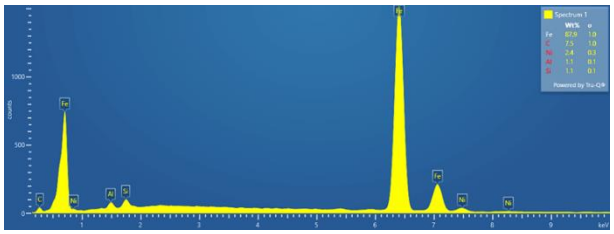

Fig. 7. EDX spectrum of sample U2-8-30.

Table 2. EDX composition of sample U2-8-30.

Element	Line Type	Weight %	Weight % Sigma	Atomic %
C	K series	7.50	0.98	26.92
Al	K series	1.14	0.14	1.83
Si	K series	1.06	0.13	1.63
Fe	K series	87.90	0.98	67.86
Ni	K series	2.39	0.28	1.76
Total		100.00		100.00

In both samples of U2-8-15 and U2-8-30, the carbon content in EDX analyses reached more than 2%, i.e. 7.83% and 7.50% respectively. The occurrence of heightened background counts in SEM-EDX often results in the emergence of a synthetic carbon (C) peak, leading to a measurement of more than 2% carbon even in the absence of actual carbon in the specimen. This occurrence is linked to the detector window, typically composed of SATW material, characterized by a specific transmission profile with a notable absorption edge just above the C X-ray energy. Consequently, an artificial peak is generated at the C energy position, primarily due to the intense absorption of background (continuum) X-rays. It is noteworthy that EDS detector manufacturers commonly employ SATW detector windows or ultrathin polymer windows produced by Moxtek [36].

3.2 Neutron Diffraction

The results of the MAUD refinement for bainitic samples U2-8-15 and U2-8-30 indicate a body-centered cubic (bcc) crystal structure with a lattice parameter of 2.7800 Å and a space group of Im$\bar{3}$m or I 4/m$\bar{3}$ 2/m. Both samples exhibit orthorhombic symmetry and a cubic crystal structure. The neutron diffraction patterns of samples U2-8-15 and U2-8-30 after refinement are shown in Fig. 8, and the overlaid diffraction patterns of the two samples are displayed in Fig. 9. Bragg's peaks or maximum intensities were observed at the planes of diffraction: (110), (200), (211), (220), and (310) for both samples, consistent with previous reports by Talebi et al. [19] and Guo et al. [37] for bainitic steel at (110), (200), (211), and (220). Table 3 provides the corresponding 2θ values of the diffraction planes for samples U2-8-15 and U2-8-30, along with their interplanar spacings. Sample U2-8-15 exhibited the highest peak intensity at the (211) plane, while sample U2-8-30 had its highest peak intensity at the (110) plane. These results provide valuable information on the crystal structure and symmetry of the bainitic steel samples derived from nickel lateritic ores.

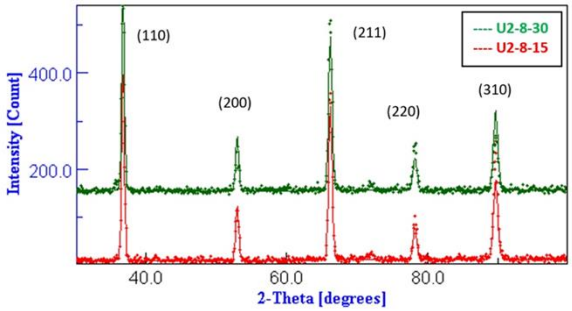

Fig. 8. Neutron diffraction patterns of samples U2-8-15 and U2-8-30.

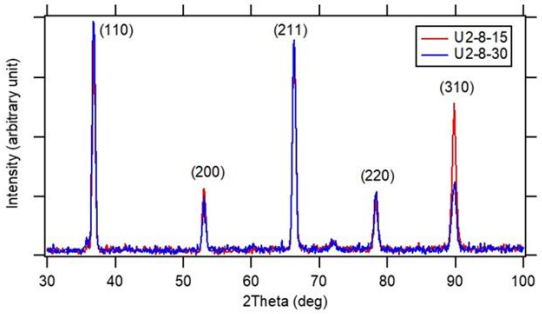

Fig. 9. The overlaid neutron diffraction patterns of samples U2-8-15 and U2-8-30.

Table 3. Diffraction planes, interplanar spacings, and two-thetas of samples U2-8-15 and U2-8-30.

(hkl)	d_1 of U2-8-15 (Å)	d_2 of U2-8-30 (Å)	$2\theta_1$ of U2-8-15 (°)	$2\theta_2$ of U2-8-30 (°)	Int_1 of U2-8-15 (%)	Int_2 of U2-8-30 (%)
(110)	2.0297	2.0284	36.757	36.781	98	100
(200)	1.4352	1.4343	52.961	52.997	29	19
(211)	1.1719	1.1711	66.197	66.248	100	90
(220)	1.0149	1.0142	78.182	78.246	22	24
(310)	0.9078	0.9071	89.650	89.738	63	27

3.3 Recalculated Pole Figures

Figs. 10 and 11 display the recalculated pole figures (RPFs) of samples U2-8-15 and U2-8-30, respectively, based on 110-, 200-, or 100-, and 211 directions. The RPFs are pole figures computed from the orientation distribution function (ODF) using LaboTex software. Comparing the RPFs of both samples, it is evident that prolonged heat treatment caused significant changes in texture or preferred orientations. The crystal orientations in sample U2-8-30 were more scattered, despite lower intensities in the RPFs (Fig. 11), indicating the breakup of texture into clusters of finer misorientations with longer heat treatment.

In sample U2-8-15, 001- or RD-textures were present in both the 110 RPF and 200 RPF (Figs. 10A and 10B). Considering the high symmetry of the cubic structure, similar textures were also expected to occur in the 00$\bar{1}$ direction in the 110 RPF and 200 RPF. However, such textures did not occur in the TD direction in the 110 RPF and 200 RPF, indicating the anisotropy of the as-cast and heat-treated sample U2-8-15. In the 110 RPF of Fig. 10A, a strong texture was observed in the 001 direction whereas slightly weaker ones were observed in the vicinities of the 340-, 010-, and $\bar{3}$ 40 directions. In contrast, in the 200 RPF of Fig. 11B, strong textures occurred in the 001-, 122-, 233-, 312-, 430-, and 140 directions. A <100> fiber texture was reported in bainite-based quenching-partitioning (BQ&P) steel under high strain rates [38]. No robust textures were observed in the 211 RPF, as shown in Fig. 11C.

Sample U2-8-30 exhibited weak and scattered textures after extended heat treatment, as shown in Figs. 11A, 11B, and 11C. However, a few strong textures were still identified in the vicinities of the 223-, 101-, and 231 directions of the 200 RPF (Fig. 11B). Other than these few strong textures, the intensity levels of textures in sample U2-8-30 were lower than those of sample U2-8-15. This phenomenon could be related to the dislocation density reduction and polygonization (recovery) of bainitic ferrite with prolonged heat treatment [39]. Dislocations in the bainite structure were reported by He et al. [40] and Cornide et al. [41]. The textures in Figs. 10 and 11 did not bear many resemblances to previous works on bainitic steels since samples U2-8-15 and U2-8-30 did not undergo plastic deformation.

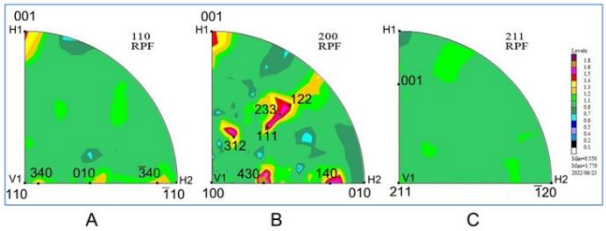

Fig. 10. The recalculated pole figures (RPFs) of sample U2-8-15 concerning A. 110 RPF, B. 200 RPF, and C. 211 RPF.

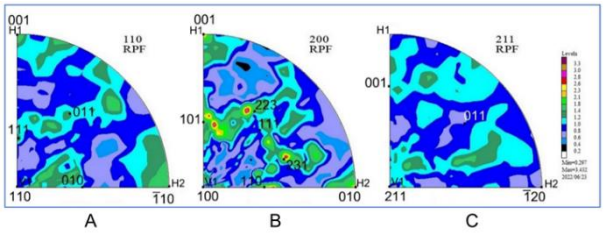

Fig. 11. The recalculated pole figures (RPFs) of sample U2-8-30 concerning A. 110 RPF, B. 200 RPF, and C. 211 RPF.

3.4 Inverse Pole Figures

Figs. 12 and 13 depict the inverse pole figures (IPF) of samples U2-8-15 and U2-8-30, respectively, based on 100-, 010-, and 001 directions. The texture evolution due to prolonged heat treatment is evident in the IPFs of both samples, with the crystal orientations of sample U2-8-30 being more scattered and lower in intensity compared to those of sample U2-8-15.

In sample U2-8-15, strong textures were observed in the 111 direction of both the 100 IPF and 010 IPF (Figs. 12A and 12B), following the trend observed in the 200 RPF of Fig. 10B. However, such a texture did not appear in the 111 direction of the 001 IPF (Fig. 12C). A strong texture in the 001 direction was also observed in the 100 IPF (Fig. 12A), corresponding to the previous 001-texture observed in the 110 RPF and 200 RPF of Figs. 10A and 10B. A texture was identified near the 213 direction in the 001 IPF, as shown in Fig. 12C.

In sample U2-8-30, most of the strong textures had vanished, although a few textures with moderate intensity were still present between the 31$\bar{2}$- and 31$\bar{3}$ directions of the 100 IPF, as shown in Fig. 13A. This phenomenon could be attributed to dislocation density reduction and polygonization of bainitic ferrite during prolonged heat treatment, leading to a decrease in texture intensity levels. The IPF textures in Figs. 12 and 13 did not exhibit similarities to any previous works on bainitic steels, possibly because the samples did not undergo plastic deformation.

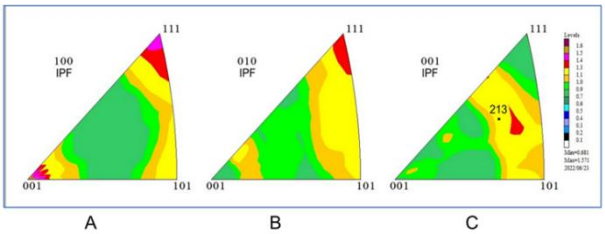

Fig. 12. Inverse pole figures (IPFs) of sample U2-8-15 concerning A. 100 IPF, B. 010 IPF, and C. 001 IPF.

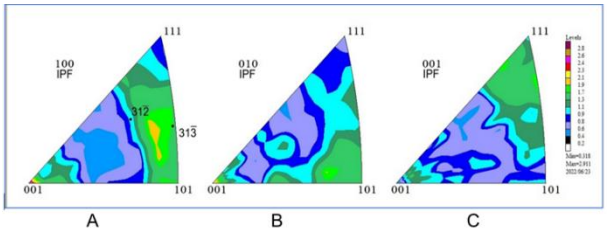

Fig. 13. Inverse pole figures (IPFs) of sample U2-8-30 concerning A. 100 IPF, B. 010 IPF, and C. 001 IPF.

3.5 Orientation Distribution Function

To convert the diffraction data into the orientation distribution function (ODF), the rotated coordinate system should first be transformed into Euler angles using the Bunge notation (φ1, Φ, φ2) [42]. Fig. 14 shows the ODF of sample U2-8-15 with a constant φ2. The ODF reveals two important aspects: texture fibers and texture components. Low-intensity textures along the λ-fiber (horizontal thick red solid lines) were detected in the range of $0° \leq \varphi2 \leq 30°$ and $80° \leq \varphi2 \leq 90°$ in sample U2-8-15. This weak λ-fiber comprised of the texture components of {001} <010> and {001} <120>. Similarly, some weak-to-moderate textures in the α-fiber (vertical thick blue dotted lines) were identified, including {113} <110> and {112} <110> texture components. These α-fiber textures occurred at $\varphi2 = 0°$, 5°, 35°, 40°, 45°, and $70° \leq \varphi2 \leq 90°$. A weak Goss texture of {110} <110> was observed and indicated by red circles. Separately, a few strong texture components of {112} <110> and {111} <11$\bar{0}$> were observed at $\varphi2 = 65°$ and $\varphi2 = 70°$, respectively.

Fig. 15 shows the ODF of sample U2-8-30. In general, all textures (fibers and texture components) of sample U2-8-30 had low intensities due to recovery (dislocation polygonization) during prolonged heat treatment. As both samples did not undergo plastic deformation, none of the typical textures observed were comparable to those from previous studies.

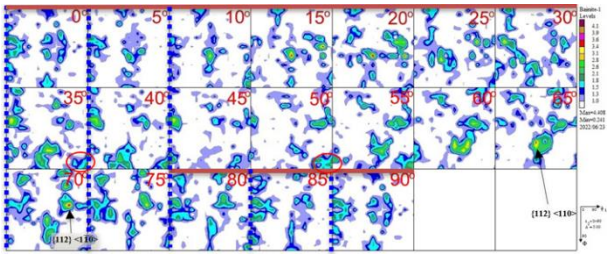

Fig. 14. ODF of sample U2-8-15 with constant ϕ2.

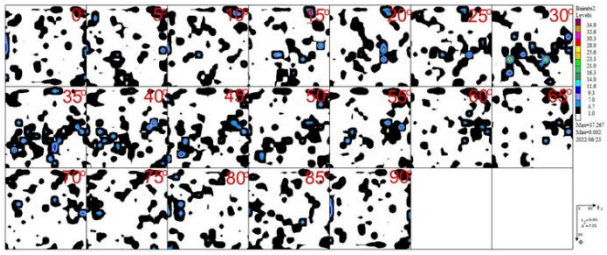

Fig. 15. ODF of sample U2-8-30 with constant ϕ2.

4 Conclusion

The study has shown that the bainitic steel processed from nickel lateritic ores exhibited diffraction patterns that followed the results of previous studies on iron-ore-based bainitic steels. The SEM/EDX analysis and observations suggest that sample U2-8-15 exhibited a bainitic microstructure due to the 15-minute heat treatment at 532°C, with the limited formation of pearlite and no significant martensite formation. Sample U2-8-30 displayed a mixed microstructure of bainite and pearlite due to the longer 30-minute heat treatment at the same temperature. The textures observed in the samples evolved from moderate in sample U2-8-15 to weak in sample U2-8-30, which was attributed to dislocation polygonization resulting from prolonged heat treatment. Few strong textures were still present in sample U2-8-15 but vanished in sample U2-8-30. The textures observed in this study did not show similarities to those from previous works due to the absence of plastic deformation leading to distinctive deformation textures. It would be interesting to investigate the texture of bainitic steels from nickel lateritic ores after undergoing plastic deformation to better understand the effects of deformation on texture development.

Declaration of Competing Interest

The authors declare that they have no known competing interests that could have appeared to influence the work reported in this paper.

Acknowledgment

The authors would like to acknowledge the Research Organization of Nuclear Technology – National Research and Innovation Agency – the Republic of Indonesia for providing grant No. B-2/III/PR/1/2022, which supported this research. We also express our gratitude to the neutron scattering laboratory of the Research Center for Radiation Detection and Nuclear Analysis Technology – National Research and Innovation Agency, Indonesia, and the ferrous materials research group of the Research Center for Metallurgy – National Research and Innovation Agency, Indonesia for their invaluable scientific and technical support throughout the study. The acquisition of samples and neutron-diffraction data was made possible thanks to their assistance.

References

1. S. Stanković et al., “Options for hydrometallurgical treatment of Ni-Co lateritic ores for sustainable supply of nickel and cobalt for European battery industry from South-Eastern Europe and Turkey,” Metals (Basel), vol. 12, no. 5, p. 807, May 2022, doi: 10.3390/met12050807.
2. J. Fraser et al., “Study on the future demand and supply security of nickel for electric vehicle batteries,” Luxembourg, Feb. 2021.
3. Y. Sun, X. Zhu, Y. Han, Y. Li, and P. Gao, “Iron recovery from refractory limonite ore using suspension magnetization roasting: A pilot-scale study,” J Clean Prod, vol. 261, p. 121221, Jul. 2020, doi: 10.1016/j.jclepro.2020.121221.
4. C. R. M. Butt and D. Cluzel, “Nickel laterite ore deposits: Weathered serpentinites,” Elements, vol. 9, no. 2, pp. 123–128, Apr. 2013, doi: 10.2113/gselements.9.2.123.

5. M. Rao, G. Li, T. Jiang, J. Luo, Y. Zhang, and X. Fan, "Carbothermic reduction of nickeliferous laterite ores for nickel pig iron production in China: A review," JOM, vol. 65, no. 11, pp. 1573–1583, Nov. 2013, doi: 10.1007/s11837-013-0760-7.
6. Y. Zhang et al., "Effects of direct reduction process on the microstructure and reduction characteristics of carbon-bearing nickel laterite ore pellets," Powder Technol, vol. 376, pp. 496–506, Oct. 2020, doi: 10.1016/j.powtec.2020.08.059.
7. Y. Xue et al., "Effective utilization of limonitic nickel laterite via pressurized densification process and its relevant mechanism," Minerals, vol. 10, no. 9, p. 750, Aug. 2020, doi: 10.3390/min10090750.
8. Z. Guo, J. Pan, D. Zhu, and F. Zhang, "Co-reduction of copper smelting slag and nickel laterite to prepare Fe-Ni-Cu alloy for weathering steel," JOM, vol. 70, no. 2, pp. 150–154, Feb. 2018, doi: 10.1007/s11837-017-2641-y.
9. H. K. D. H. Bhadeshia, "A personal commentary on 'transformation of austenite at constant subcritical temperatures,'" Metallurgical and Materials Transactions A, vol. 41, no. 6, pp. 1351–1390, Jun. 2010, doi: 10.1007/s11661-010-0250-2.
10. J. B. AUSTIN, "EDGAR COLLINS BAIN," Biographical Memoirs, vol. 50, p. 25, 1978.
11. H. K. D. H. Bhadeshia and R. W. K. Honeycombe, Steels: microstructures and properties. Butterworth-Heinemann, 2017.
12. H. Matsuda and H. K. D. H. Bhadeshia, "Kinetics of the bainite transformation," Proceedings of the Royal Society of London. Series A: Mathematical, Physical and Engineering Sciences, vol. 460, no. 2046, pp. 1707–1722, Jun. 2004, doi: 10.1098/rspa.2003.1225.
13. A. Kumar, S. B. Singh, and K. K. Ray, "Influence of bainite/martensite-content on the tensile properties of low carbon dual-phase steels," Materials Science and Engineering: A, vol. 474, no. 1–2, pp. 270–282, Feb. 2008, doi: 10.1016/j.msea.2007.05.007.
14. A. Eres-Castellanos, L. Morales-Rivas, F. G. Caballero, and C. Garcia-Mateo, "Explaining the dilatometric behavior during bainite transformation under the effect of variant selection," J Alloys Compd, vol. 864, p. 158130, May 2021, doi: 10.1016/j.jallcom.2020.158130.
15. L. Morales-Rivas et al., "Crystallographic examination of the interaction between texture evolution, mechanically induced martensitic transformation and twinning in nanostructured bainite," J Alloys Compd, vol. 752, pp. 505–519, Jul. 2018, doi: 10.1016/j.jallcom.2018.04.189.
16. A. Eres-Castellanos, L. Morales-Rivas, J. A. Jimenez, F. G. Caballero, and C. Garcia-Mateo, "Effect of ausforming on the macro- and micro-texture of bainitic microstructures," Metallurgical and Materials Transactions A, vol. 52, no. 9, pp. 4033–4052, Sep. 2021, doi: 10.1007/s11661-021-06363-w.
17. J. Li, F. Liu, S. Wang, J. Li, Y. Liu, and Q. Meng, "Effect of two-step bainite treatment on the morphology and texture of retained austenite and mechanical properties of austenitizing pretreated transformation-induced plasticity steel," Materials Science and Engineering: A, vol. 771, p. 138567, Jan. 2020, doi: 10.1016/j.msea.2019.138567.
18. S. Kundu, K. Hase, and H. K. D. H. Bhadeshia, "Crystallographic texture of stress-affected bainite," Proceedings of the Royal Society A: Mathematical, Physical and Engineering Sciences, vol. 463, no. 2085, pp. 2309–2328, Sep. 2007, doi: 10.1098/rspa.2007.1881.
19. S. Z. Shuja, B. S. Yilbas, and S. Z. Shazli, "Laser repetitive pulse heating influence of pulse duty on temperature rise," Heat and Mass Transfer, vol. 43, no. 9, pp. 949–955, Jul. 2007, doi: 10.1007/s00231-006-0168-9.
20. Structural alloys for power plants. Elsevier, 2014. doi: 10.1016/C2013-0-16201-0.
21. Z. Dai et al., "Fundamentals and application of solid-state phase transformations for advanced high strength steels containing metastable retained austenite," Materials Science and Engineering: R: Reports, vol. 143, p. 100590, Jan. 2021, doi: 10.1016/j.mser.2020.100590.
22. M. Soleimani, A. Kalhor, and H. Mirzadeh, "Transformation-induced plasticity (TRIP) in advanced steels: A review," Materials Science and Engineering: A, vol. 795, p. 140023, Sep. 2020, doi: 10.1016/j.msea.2020.140023.
23. S. W. Thompson, D. J. Colvin, and G. Krauss, "Austenite decomposition during continuous cooling of an HSLA-80 plate steel," Metallurgical and Materials Transactions A, vol. 27, no. 6, pp. 1557–1571, Jun. 1996, doi: 10.1007/BF02649815.
24. H. R. K. Zarchi, A. Khajesarvi, S. S. G. Banadkouki, and M. C. Somani, "Microstructural evolution and carbon partitioning in interstitial free weld simulated API 5L X60 steel," REVIEWS ON ADVANCED MATERIALS SCIENCE, vol. 58, no. 1, pp. 206–217, Nov. 2019, doi: 10.1515/rams-2019-0016.
25. M. Naderi, M. Ketabchi, M. Abbasi, and W. Bleck, "Analysis of microstructure and mechanical properties of different high strength carbon steels after hot stamping," J Mater Process Technol, vol. 211, no. 6, pp. 1117–1125, Jun. 2011, doi: 10.1016/j.jmatprotec.2011.01.015.
26. S.-I. Lee et al., "Influence of austempering temperature on microstructure and mechanical properties of high-carbon nanostructured bainitic steels," Materials Science and Engineering: A, vol. 848, p. 143334, Jul. 2022, doi: 10.1016/j.msea.2022.143334.
27. L. Stratil, V. Horník, P. Dymáček, P. Roupcová, and J. Svoboda, "The influence of aluminum content on the oxidation resistance of new-generation ODS

alloy at 1200 °C," Metals (Basel), vol. 10, no. 11, p. 1478, Nov. 2020, doi: 10.3390/met10111478.

28. J. S. Dunning, D. E. Alman, and J. C. Rawers, "Influence of silicon and aluminum additions on the oxidation resistance of lean-chromium stainless steel," Oxidation of Metals, vol. 57, no. 5/6, pp. 409–425, 2002, doi: 10.1023/A:1015344220073.
29. M. Acarer and B. Demir, "An investigation of mechanical and metallurgical properties of explosive welded aluminum–dual phase steel," Mater Lett, vol. 62, no. 25, pp. 4158–4160, Sep. 2008, doi: 10.1016/j.matlet.2008.05.060.
30. R. Guluzade, A. Avcı, M. Turan Demirci, and Ö. Faruk Erkendirci, "Fracture toughness of recycled AISI 1040 steel chip reinforced AlMg1SiCu aluminum chip composites," Materials & Design (1980-2015), vol. 52, pp. 345–352, Dec. 2013, doi: 10.1016/j.matdes.2013.05.025.
31. L. H. Shah and M. Ishak, "Review of research progress on aluminum–steel dissimilar welding," Materials and Manufacturing Processes, vol. 29, no. 8, pp. 928–933, Aug. 2014, doi: 10.1080/10426914.2014.880461.
32. M. Khandaei, Y. Vahidshad, and M. Ayaz, "Improvement of weld quality in electromagnetic welding of aluminum-stainless steel sheets," Materwiss Werksttech, vol. 51, no. 10, pp. 1372–1388, Oct. 2020, doi: 10.1002/mawe.201900205.
33. Y. Sun, S. Hu, Z. Xiao, S. You, J. Zhao, and Y. Lv, "Effects of nickel on low-temperature impact toughness and corrosion resistance of high-ductility ductile iron," Mater Des, vol. 41, pp. 37–42, Oct. 2012, doi: 10.1016/j.matdes.2012.03.039.
34. G. R. Thellaputta, P. S. Chandra, and C. S. P. Rao, "Machinability of nickel-based superalloys: A review," Mater Today Proc, vol. 4, no. 2, pp. 3712–3721, 2017, doi: 10.1016/j.matpr.2017.02.266.
35. T. Sarvar, T. Nodir, and O. Furkat, "Silicon as an alloying element in steels," Asian Journal Of Multidimensional Research, vol. 11, no. 9, pp. 71–74, 2022, doi: 10.5958/2278-4853.2022.00214.2.
36. Y. Liao, "EDS measurement of carbon: practical electron microscopy and database," https://www.globalsino.com/EM/page1853.html.
37. Y. Guo et al., "Microstructure evolution of Fe-based nanostructured bainite coating by laser cladding," Mater Des, vol. 63, pp. 100–108, Nov. 2014, doi: 10.1016/j.matdes.2014.05.041.
38. X. Wu, F. Jiang, Z. Wang, D. Yuan, G. Gao, and C. Guo, "Mechanical behavior and microstructural evolution of a bainite-based quenching-partitioning (BQ&P) steel under high strain rates," Materials Science and Engineering: A, vol. 818, p. 141414, Jun. 2021, doi: 10.1016/j.msea.2021.141414.
39. Z. Ławrynowicz, "Bainitic reaction and microstructure evolution in two normalized and tempered steels designed for service at elevated temperatures," Advances in Materials Science, vol. 17, no. 4, pp. 22–36, Dec. 2017, doi: 10.1515/adms-2017-0019.
40. S. H. He, B. B. He, K. Y. Zhu, and M. X. Huang, "Evolution of dislocation density in bainitic steel: Modeling and experiments," Acta Mater, vol. 149, pp. 46–56, May 2018, doi: 10.1016/j.actamat.2018.02.023.
41. J. Cornide, G. Miyamoto, F. G. Caballero, T. Furuhara, M. K. Miller, and C. García-Mateo, "Distribution of dislocations in nanostructured bainite," Solid State Phenomena, vol. 172–174, pp. 117–122, Jun. 2011, doi: 10.4028/www.scientific.net/SSP.172-174.117.
42. H.-J. Bunge, "Zur darstellung allgemeiner texturen," International Journal of Materials Research, vol. 56, no. 12, pp. 872–874, Dec. 1965, doi: 10.1515/ijmr-1965-561213.